

Supporting Information - Measuring spatially resolved collective ionic transport on lithium battery cathodes using atomic force microscopy

Aaron Mascaro,^{*,†} Zi Wang,[‡] Pierre Hovington,[¶] Yoichi Miyahara,[†] Andrea
Paolella,[¶] Vincent Gariepy,[¶] Zimin Feng,[¶] Tyler Enright,[†] Connor Aiken,[†] Karim
Zaghib,[¶] Kirk H. Bevan,[‡] and Peter Grutter[†]

*Department of Physics, McGill University, 3600 rue University, Montreal, Québec H3A2T8,
Canada, Materials Engineering, McGill University, 3610 rue University, Montreal, Québec
H3A0C5, Canada, and Institut de Recherche d'Hydro Québec, 1800 Boulevard Lionel-Boulet,
Varennnes, Québec J3X1S1, Canada*

E-mail: mascaroa@physics.mcgill.ca

^{*}To whom correspondence should be addressed

[†]Department of Physics, McGill University

[‡]Materials Engineering, McGill University

[¶]Institut de Recherche d'Hydro Québec

Experimental Methods

Atomic Force Microscopy Measurements. The AFM measurements were performed using a highly customized JSPM-5200 microscope (including a custom fabricated sample heater stage) operating in high vacuum (10^{-7} mBar) with a gold-coated tip ($r = 20$ nm, $k = 231$ N/m, $f_0 = 1.227$ MHz, $A_{pp} \approx 12$ nm for the platelet measurements; and $r = 20$ nm, $k = 27$ N/m, $f_0 = 296$ kHz, $A_{pp} \approx 5$ nm for the ingot measurements) controlled using GXSM.¹ A Nanosurf[®] EasyPLL Plus was used in the standard FM-AFM self-excitation configuration during scanning for the ingot sample measurements.² Topography images on the LiFePO_4 platelets were obtained in high vacuum using Q-control to decrease the effective quality factor.³ KPFM was performed using the sideband detection scheme with an external PLL and PID controller (Zurich Instruments HF2) with a modulation amplitude of 2 V and modulation frequency of 800 Hz, as described elsewhere.⁴ The V_{dc} was applied to the tip while the sample was grounded, resulting in a V_{cpd} value with the opposite sign as the difference in work function (sample-tip) so that the regions of high V_{cpd} in the KPFM image actually correspond to a lower sample work function (see Figure S5).

A simple understanding of the ionic response starts with the general expression for the electrostatic force between a conducting AFM tip and a sample:

$$F = \frac{1}{2} \frac{\partial C}{\partial z} V^2 \quad (\text{S } 1)$$

If the tip is separated from the back electrode by a vacuum gap (between the tip and sample) and a dielectric sample, the series capacitance is:

$$C = \frac{1}{\frac{1}{C_v} + \frac{1}{C_\epsilon}} \quad (\text{S } 2)$$

where C_v is the vacuum capacitance and C_ϵ is the capacitance of the dielectric. In the case where the ions fully screen the internal field after some saturation time (t_s), the capacitance of the dielectric goes to infinity, so the overall capacitance $C \rightarrow C_v$. Due to the small distance between the tip and

surface of the sample, C_v is much more sensitive to z-position than C_s , so $\frac{\partial C}{\partial z}$ increases. Thus, the electrostatic force will increase until the saturation time is reached. Since this process is due to ions hopping through a lattice on long timescales, the electrostatic force follows Eq. 2.

The time trace frequency shift data was fitted to Eq. SS 3, where df_0 is the initial frequency shift and df_s is the final (saturation) frequency shift.

$$df(t) = df_0 + df_s \exp[-(t/\tau)^\beta] \quad (\text{S } 3)$$

The time constants were then fitted to Eq. 3 to determine activation energies and effective attempt frequencies for each probe-point. The bulk ionic hopping barriers were found using Eq. 4.

The optimal time resolution attainable (i.e. the fastest change in frequency that can be recorded) in FM-AFM is usually limited by the frequency detector (typically a phase-locked-loop, PLL), which has a finite response time to instantaneous frequency changes. In order to decrease this response time, the frequency detection bandwidth (and hence the overall input noise) must be increased. To achieve sub-millisecond time resolution, we developed a system that acquires a repeated signal and averages it in real-time until an acceptable noise level is achieved. To perform the relaxation-time measurements an external PLL (Zurich Instruments HF2) was used as a frequency detector with the bandwidth set to 4 kHz to realize a $\approx 150\mu$ s response time for measurements on the ingot sample and a 10 kHz bandwidth with response time $\approx 60\mu$ s for the platelet samples. This high (10kHz) bandwidth was achieved using ultra-high frequency cantilevers with \sim MHz resonance frequencies and allows for time resolution limited only by the real-time averaging system. To achieve acceptable SNR, each measurement was averaged over $N = 100$ to $N = 700$ pulses by an on-line data processing system to acquire and average the data in real-time (developed using Mathworks[®] Simulink Real-Time[®] and running at a base sample rate of 20 kHz). The pulses were applied using a signal generator triggered by the SPM scan controller (Soft dB MK2-A810) for 40 ms. The measurements at each point/temperature were performed 10 times in order to calculate a statistical error value. Before each probe measurement, the initial V_{dc} was set to the contact

potential difference, V_{cpd} , by sweeping V_{dc} to find the minimum in the parabolic Δf - V_{dc} curve.

Kelvin Probe Force Microscopy. In general, the electrostatic force between an AFM tip and a sample is given by:

$$F_{es} = \frac{1}{2} \frac{\partial C}{\partial z} \Delta V^2 \quad (\text{S } 4)$$

where C is the tip-sample capacitance, z is the tip-sample separation, and ΔV is the potential difference between the tip and sample. The contact potential difference is defined by:

$$V_{cpd} = \frac{\phi_{tip} - \phi_{sample}}{-e} \quad (\text{S } 5)$$

where ϕ refers to the work function of the materials and e is the electron charge. Thus, if we apply both a V_{dc} and a V_{ac} (at some frequency ω) between the tip and sample, the total voltage difference is given by:

$$\Delta V = V_{dc} - V_{cpd} + V_{ac} \sin(\omega t) \quad (\text{S } 6)$$

Inserting this into Eq. S 4, expanding, and simplifying, we see that there are three frequency components of the overall electrostatic force:

$$F_{dc} = \frac{\partial C}{\partial z} \left[\frac{1}{2} (V_{dc} - V_{cpd})^2 + \frac{1}{4} V_{ac}^2 \right] \quad (\text{S } 7)$$

$$F_{\omega} = \frac{\partial C}{\partial z} [V_{dc} - V_{cpd}] V_{ac} \sin(\omega t) \quad (\text{S } 8)$$

$$F_{2\omega} = \frac{1}{4} \frac{\partial C}{\partial z} V_{ac}^2 \cos(2\omega t) \quad (\text{S } 9)$$

The ω component of the force, F_{ω} , is what is used in KPFM; we can clearly see that when $V_{dc} = V_{cpd}$, F_{ω} is zero. By controlling V_{dc} with a feedback loop such that $F_{\omega} = 0$, we achieve $V_{dc} = V_{cpd}$ and thus V_{cpd} can be measured.

While the V_{cpd} is proportional to the difference in work functions between the tip and sample, the absolute value of these work functions cannot be easily determined due to a variety of fac-

tors, including difficulty in determining the exact tip work function (see⁵ for a discussion of other challenges). In our case the V_{cpd} has the opposite sign of the measured voltage so that the regions of lower work function on the sample have higher V_{cpd} in Figure S4. This is due to the voltage (V_{dc}) measurement being taken from the tip potential while the sample is grounded. This can be better understood by drawing an energy level diagram as shown in Figure S5.⁶ Performing KPFM on a thick insulating sample with a high dielectric constant such as LiFePO_4 further complicates quantitative analysis as the voltage decay within the sample also has to be taken into account. The ϕ_{sample} has to be referred to the Fermi level of the back-electrode material, thus the V_{cpd} variations along the surface will be a fraction of the true work function variations of the sample. The large capacitive force present between the macroscopic parts of the probe (namely the cantilever) also contribute to a complicated electrostatics problem with dependencies on not only the applied voltages and geometries, but also the tip oscillation amplitude.⁷

Data analysis. For each probe point 10 measurements were conducted at each temperature. After fitting the frequency shift vs. time data to Eq. SS 3 to extract the relaxation times, τ , and stretching factor, β , the collective activation energies were obtained by a linear fit to the natural log of the relaxation times vs. energies as per Eq. 3 (i.e. the linear fit shown in Figure 2C). Parametric bootstrap was used to determine an estimate for the uncertainty on the activation energies, β , and τ_∞ using a Gaussian distribution with the mean and standard deviation of each data point and 1000 iterations.⁸ A non-parametric bootstrap was performed for several points, but yielded the same uncertainty on the fit parameters to the indicated significance and thus a parametric bootstrap was used to minimize computation time.

TOF-SIMS. The Time of Flight Secondary Ion Mass (TOF-SIMS) analyses were performed using the Tescan Lyra3 FIB/SEM microscope fitted with a TOF-SIMS from TOFWERK. A focus ion beam (Ga) with an ion current of 1.7 nA was used to sputter the secondary ions in an area with a field of view of 18 μm (768×768 pixels). Electron beam flooding was used to minimize charging effects and obtain a reasonable SNR (spot mode, 2nA current at 5kV). The sample surface

was normal to the ion beam. Each of the 7 frames recorded is composed of 768×768 extractions with a FIB dwell time of $10 \mu s$ per pixel. The final image was binned 4 times (192×192 pixels). See Figure S7 for depth profiles and mass/charge spectra. The ion current and analyzed area were chosen so the features of interest were still visible after the analysis (quasi static mode). The voltage on the TOF-SIMS plates was selected so only the positive ions were measured.

EBSD. The ingot sample was ion milled (Hitachi IR4000+) using 3 kV Ar^+ for 3 minutes to minimize any residual stress at the sample surface. The sample was then glued onto a pre-tilted (70°) sample holder and analyzed in a Lyra3 microscope using a 20 kV electron beam. The EBSD detector utilized the Aztec software and NordlysNano camera (Oxford Instruments) to record the pattern. Both mapping (1 frame per second) and point analysis were used to determine the crystallographic orientation of the same region of interest that was measured using TOF-SIMS and on several LiFePO_4 platelet samples. The EBSD measurement on the ingot sample was performed after the TOF-SIMS measurement on the region of interest, which left the surface especially rough in the center grain (region B), while the outer regions remained relatively smooth. This roughness prevented a reasonable signal from being obtained on the center region, thus the indexation was not reliable and is therefore not reported here.

***Ab initio* calculations.** The *ab initio* calculations were performed using the GGA functional by Perdew, Burke, and Ernzerhof (PBE)⁹ within the projector augmented wave (PAW) formalism¹⁰ as implemented in the Vienna *ab initio* simulation package (VASP).^{11–14} To account for the strong electron correlation present in the Fe 3d orbitals, an on-site Hubbard term U was added to the functional (GGA + U). The value of U depends on the material and the oxidation state of the Fe atoms, which we selected to be $U_{\text{eff}} = 3.7$ eV for pure LiFePO_4 , $U_{\text{eff}} = 4.9$ eV for pure FePO_4 , and $U_{\text{eff}} = 4.3$ eV for systems with mixed oxidation states.^{15,16}

Ionic diffusion calculations were done on $1 \times 4 \times 2$ supercells with a plane wave energy cutoff of 500 eV and a single k-point at the Γ -point in reciprocal space. The dimensions of the supercells were set to simulate a concentration of $x = 0.75$, with the lattice vectors assumed to be a linear

combination of 25% FePO_4 and 75% LiFePO_4 lattice vectors. To simulate a phase boundary between LiFePO_4 and FePO_4 , one half of the supercells were fully lithiated (with Fe sites reduced to 2+), and the other half empty (with the oxidation state of the Fe sites at 3+). To simulate interactions in a dilute phase, a system was studied where only two Li ions (and two polarons) are introduced in an otherwise fully delithiated supercell. The lowest energy configuration of this system was found through enumeration of all possible symmetrically distinct configurations. Internal coordinates were fully relaxed. To calculate diffusion barriers, we utilized the climbing image nudged elastic band method (CI-NEB)^{17,18} to optimize the images between endpoints.

To the best of our knowledge, the experimental reference values of the work functions of LiFePO_4 and FePO_4 are not available. Therefore, we investigated the work functions of LiFePO_4 and FePO_4 from an *ab initio* approach. Since the work functions of different surface orientations of the same material will not vary significantly (usually within a few tenth of eV, as confirmed by our calculations of two other surface orientations of FePO_4), we chose the (010) orientation, which has the lowest surface energy,¹⁹ as the characteristic surface for our calculation. A 20 Å thick slab of $\text{LiFePO}_4/\text{FePO}_4$ separated by a vacuum layer with a thickness of 40 Å was used in the study. By comparing the reported results with the those corresponding to slightly smaller thicknesses, our results appear to be converged.

Materials Preparation

LiFePO_4 platelets were synthesized following a hydrothermal route (reported in Ref.²⁰): 33.6 g (0.12 mol) $\text{FeSO}_4 \cdot 7\text{H}_2\text{O}$, 15.41 g (0.36 mol) $\text{LiOH} \cdot \text{H}_2\text{O}$, 13.83 g (0.12 mol) H_3PO_4 , and 0.5 g (0.003 mol) ascorbic acid ($\text{C}_6\text{H}_8\text{O}_6$) were mixed with 300 ml of deionised water in a glass liner. The final molar ratio for $\text{Li}:\text{Fe}:\text{PO}_4:\text{C}_6\text{H}_8\text{O}_6$ was 3:1:1:0.008. The pH was controlled at 7.8 by drop-wise addition of NH_4OH . The synthesis was performed in a stirred autoclave (OM-JAPAN) for 5 hours at 180 °C. The resulting platelets at this stage were dispersed in Milli-Q water and drop cast onto a template stripped gold substrate. These platelets were used for the measurements shown in Figure 1.

To prepare the ingot sample, the platelets were then ground for 30 minutes with a SPEX[®] grinder prior to delithiation. The LiFePO_4 crystals were dispersed in potassium persulfate ($\text{K}_2\text{S}_2\text{O}_8$) water solution (molar ratio 2:1) and heated at 60 °C for 24 hours to promote the final Li_xFePO_4 conversion.^{21,22} Finally, the powder was held at 1050 °C under N_2 for 1 hour to obtain a bulk sample, which was polished using successive diamond abrasive papers from 30 μm down to 0.3 μm particle size.

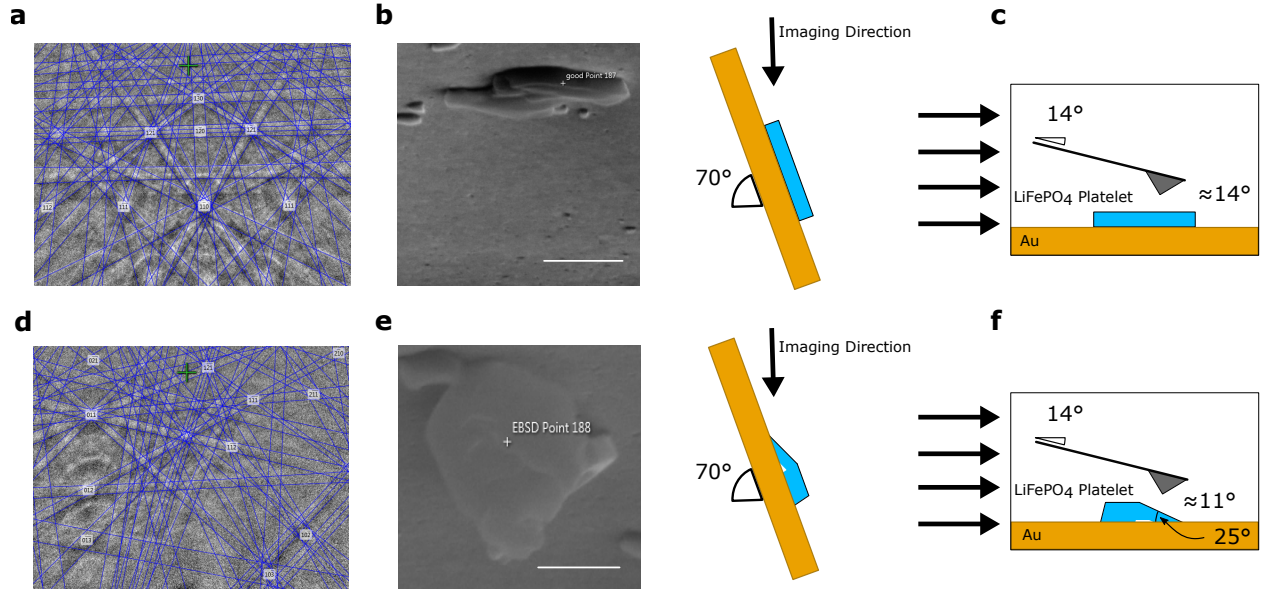


Figure S 1: **(a)** Indexed Kikuchi pattern from EBSD conducted on platelet shown in **(b)**. This pattern confirms that the (010) axis is directly perpendicular to the surface as shown in Figure 1A. **(b)** SEM image taken of a LiFePO_4 platelet on a gold substrate while oriented for EBSD measurement at a 70° angle as shown in illustration, scale bar $2\mu\text{m}$. **(c)**. Illustration of the orientation of the AFM cantilever with respect to the platelet and gold substrate. The nominal angle between the normal direction from the surface to the tip-axis of the cantilever is $\approx 14^\circ$. **(d)** Indexed Kikuchi pattern from EBSD conducted on platelet shown in **(e)**, where it is clear that the platelet is not perfectly oriented along the gold surface. **(e)** shows an SEM image of the platelet taken in the EBSD orientation, as illustrated. From this image and the Kikuchi pattern we determined that the (010) axis is perfectly perpendicular to the surface of the platelet and the platelet is oriented at $\approx 25^\circ$ from the gold surface, as illustrated in **(f)**. The nominal angle between the normal direction from the platelet surface to the tip-axis of the cantilever is $\approx 11^\circ$, shown in **(f)**

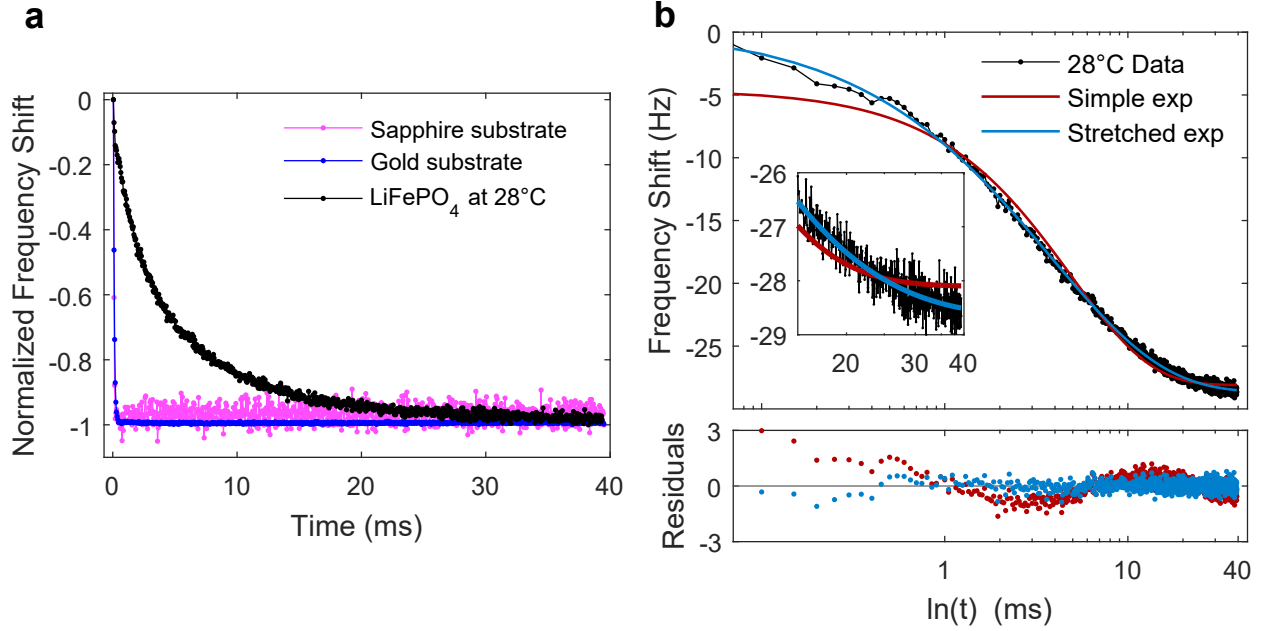


Figure S 2: Ionic response validation measurements. **(a)** Normalized frequency shift vs. time for probe measurements performed on 430 μ m thick single crystal sapphire, gold, and the LiFePO₄ platelet shown in Figure 1E all conducted under the same conditions using the same cantilever. **(b)** Result of fitting the data shown in **(a)** taken on the LiFePO₄ sample to a pure exponential (red line) and a stretched exponential (blue line) with residuals from both fits shown below. Both plots are linear-log to better display the poor fit of the pure exponential function. A χ^2 test on the residuals reveals that the pure exponential residuals are not normally distributed ($p = 0.03$), while the residuals for the stretched exponential fit are normally distributed ($p = 0.17$). Inset shows a close-up from 10-40ms, also as a linear-log plot.

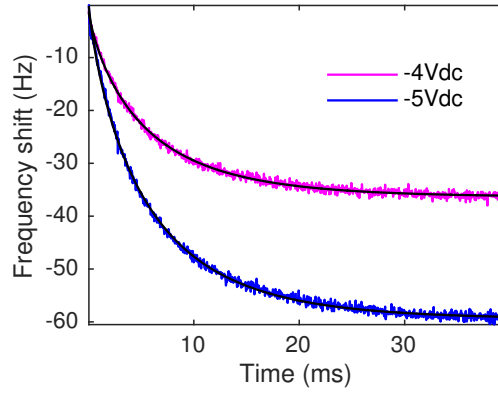


Figure S 3: Probe measurements taken on the same point with two different V_{dc} values (-4V and -5V as indicated). Black lines are fits to each curve. The parameters obtained from the fitting are: 5.46 ± 0.07 ms and 5.38 ± 0.11 ms; and 0.80 ± 0.03 and 0.80 ± 0.04 for -5V applied and -4V applied, respectively.

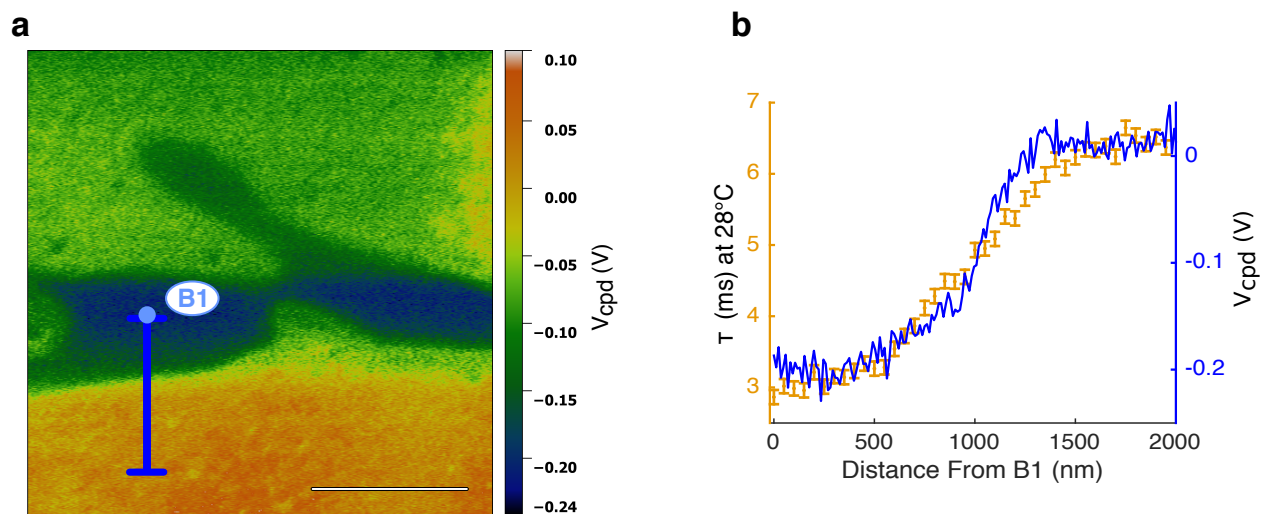


Figure S 4: (a) Kelvin Probe Force Microscopy (KPFM) taken simultaneously with FM-AFM topography, scale bar is $2\mu\text{m}$. (b) Surface contact potential difference data along the line indicated in (a) plotted on top of the relaxation time constants at each point spaced 50nm apart.

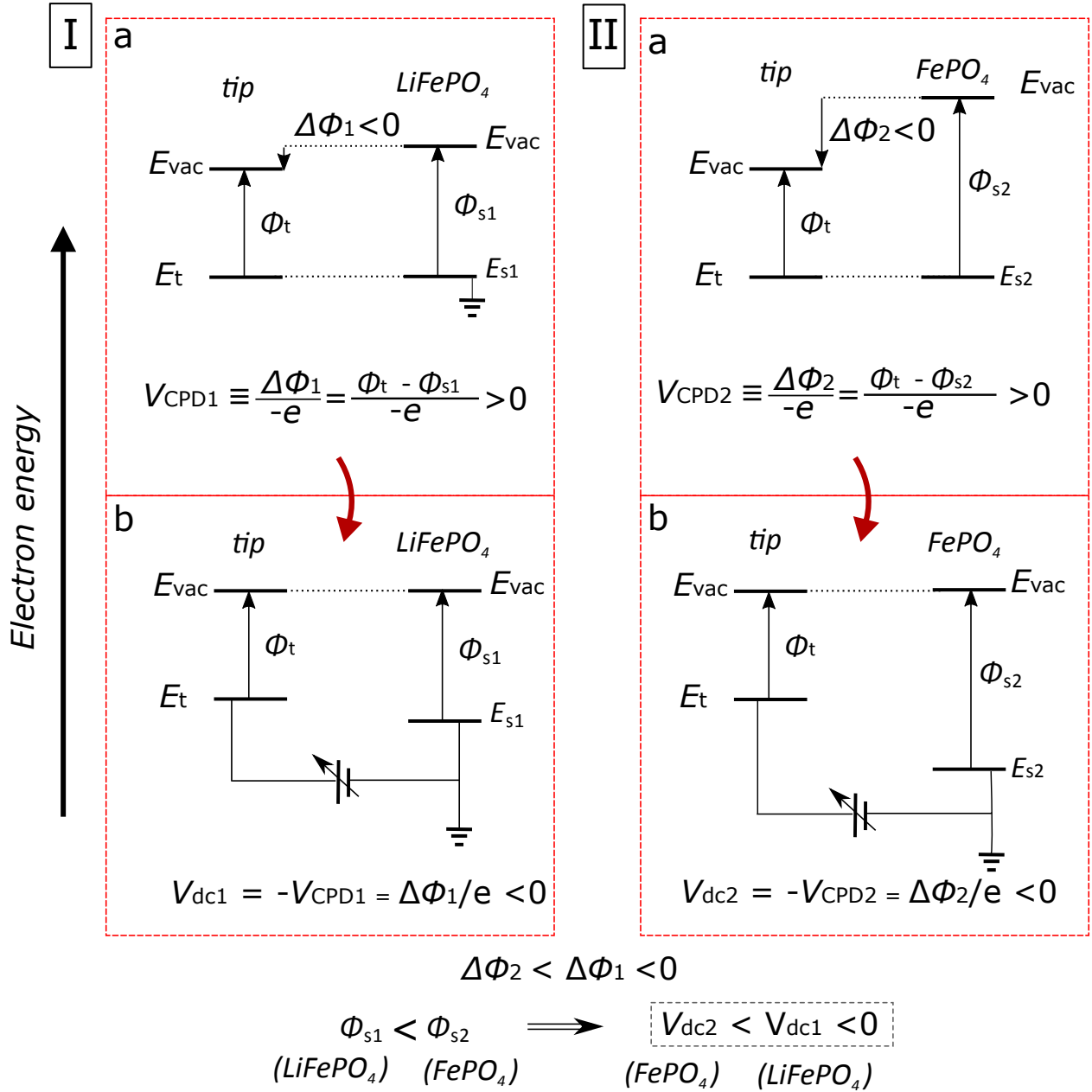


Figure S 5: Tip-sample energy level diagrams for the $LiFePO_4$ and $FePO_4$ sample phases. The work functions of $LiFePO_4$ and $FePO_4$ are 5.2eV (ϕ_{s1}) and 8.3eV (ϕ_{s2}), respectively (see main text). Thus, for $LiFePO_4$ (case I) the sample has a lower work function (ϕ_{s1}), which results in a more positive V_{dc} . $FePO_4$ has a higher work function (ϕ_{s2} , case II), giving a more negative V_{dc} . For each case the (a) panel corresponds to the initial energy levels with no bias applied, while (b) gives the energy levels during the KPFM measurement.

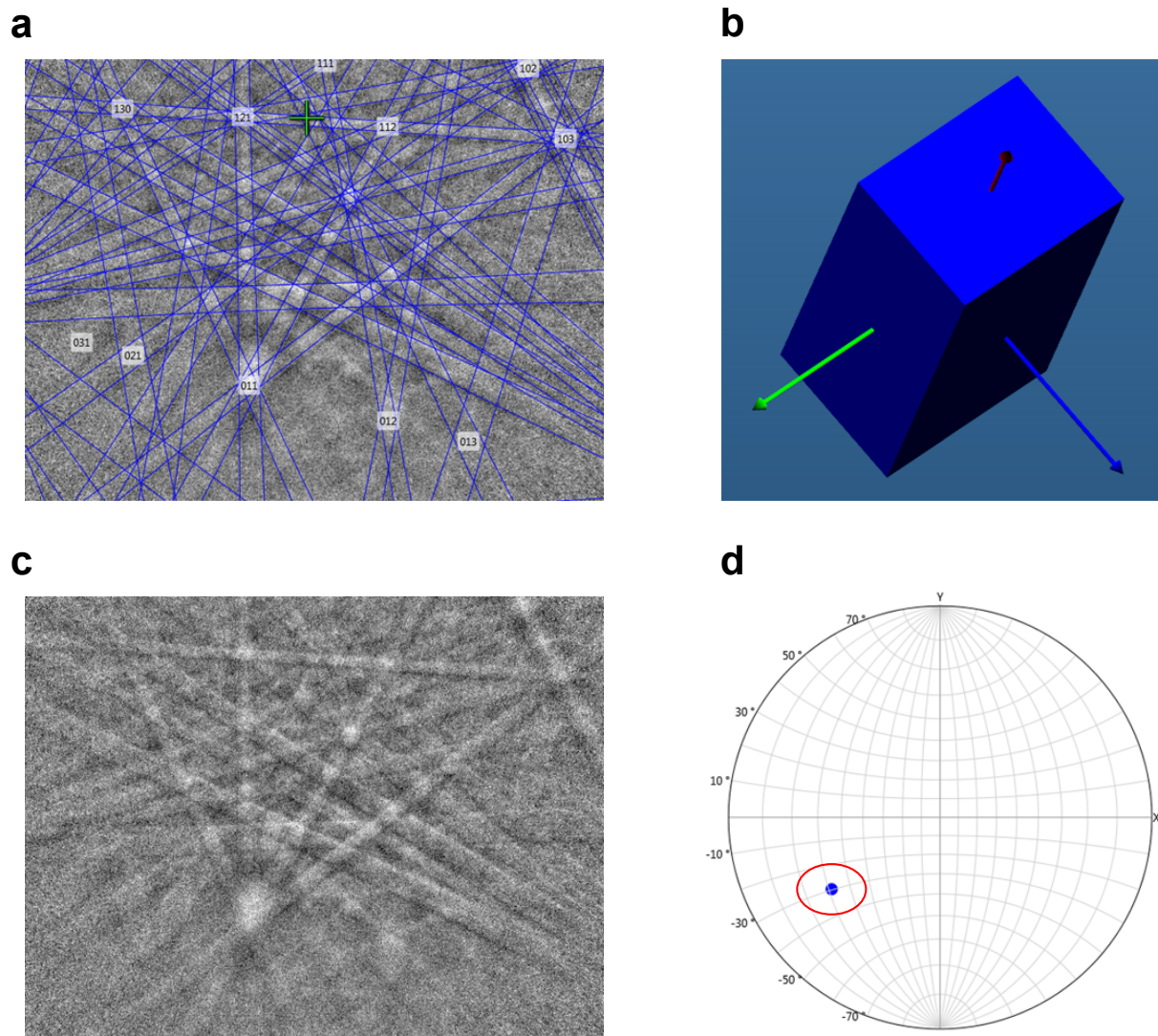


Figure S 6: **(a)** Indexed Kikuchi pattern of LiFePO_4 phase on partially delithiated ingot sample. **(b)** Crystallographic orientation determined from Kikuchi pattern. **(c)** Raw Kikuchi pattern. **(d)** Pole plot of (010) axis showing orientations obtained from EBSD mapping over the LiFePO_4 region, circled in red.

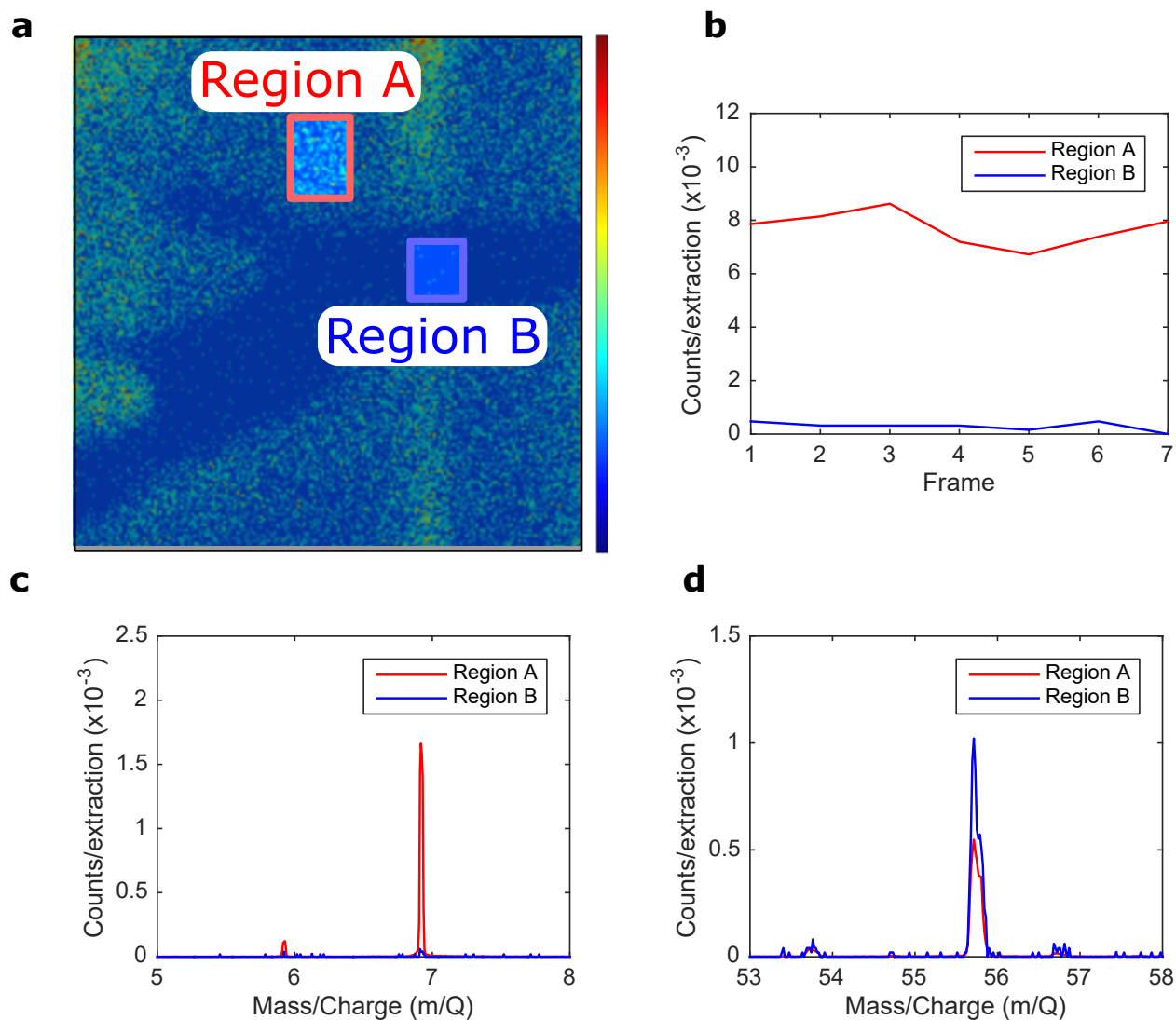


Figure S 7: **(a)** TOF-SIMS mapping on the partially delithiated LiFePO_4 ingot sample with a high Li^+ concentration region (A) and a low Li^+ concentration region (B) outlined for analysis. Colour scale extends from 0 to 0.08 counts/TOF-SIMS extraction. **(b)** Counts/TOF-SIMS extraction of the indicated regions as a function of depth over all frames acquired. **(c)** Mass spectra of both regions A and B showing the ${}^6\text{Li}^+$ and ${}^7\text{Li}^+$ peaks. **(d)** Mass spectra of both regions A and B showing the ${}^{56}\text{Fe}^+$ peaks.

Table S 1: Results obtained from both points indicated on the LiFePO_4 platelet shown in Figure 1E in the main text. Uncertainty of values obtained from fitting are the standard deviation values obtained from bootstrapping (see methods).

Point	1	2
E_a^* (eV)	0.44(7)	0.49(3)
E_a (eV)	0.26(4)	0.34(2)
β	0.59(1)	0.69(1)
τ_∞ (s)	$2(2) \times 10^{-9}$	$5(7) \times 10^{-11}$
Collective Diffusivity (cm^2/s)	$3.7(4) \times 10^{-13}$	$1.90(7) \times 10^{-13}$
Bulk Diffusivity (cm^2/s)	$(0.2 \pm 2.0) \times 10^{-10}$	$3(5) \times 10^{-11}$

Table S 2: Results obtained at each of the 6 probe-points in order by region, top to bottom. Uncertainty of values obtained from fitting are the standard deviation values obtained from the Monte Carlo simulations (see Methods).

Point	A1	A2	B1	B2	C1	C2
E_a^* (eV)	0.54(2)	0.54(2)	0.62(3)	0.62(3)	0.49(1)	0.52(1)
E_a (eV)	0.30(1)	0.30(1)	0.36(1)	0.38(1)	0.31(1)	0.33(1)
β	0.565(5)	0.548(5)	0.572(4)	0.614(5)	0.628(4)	0.649(6)
τ_∞ (s)	5(3) $\times 10^{-12}$	5(5) $\times 10^{-12}$	2(3) $\times 10^{-13}$	2(3) $\times 10^{-13}$	6(3) $\times 10^{-11}$	2(1) $\times 10^{-11}$
Collective Diffusivity (cm ² /s)	2.31(7) $\times 10^{-13}$	2.31(7) $\times 10^{-13}$	2.27(7) $\times 10^{-13}$	2.27(8) $\times 10^{-13}$	1.05(2) $\times 10^{-13}$	1.10(2) $\times 10^{-13}$
Bulk Diffusivity (cm ² /s)	1(1) $\times 10^{-9}$	2(2) $\times 10^{-9}$	4(6) $\times 10^{-9}$	2(2) $\times 10^{-9}$	1.1(6) $\times 10^{-10}$	1.1(6) $\times 10^{-10}$

References

- (1) Zahl, P.; Bierkandt, M.; Schröder, S.; Klust, A. *Rev. Sci. Instrum.* **2003**, *74*, 1222–1227.
- (2) Albrecht, T.; Grütter, P.; Horne, D.; Rugar, D. *J. Appl. Phys.* **1991**, *69*, 668–673.
- (3) Anczykowski, B.; Cleveland, J.; Krüger, D.; Elings, V.; Fuchs, H. *Appl. Phys. A: Mater. Sci. Process.* **1998**, *66*, S885–S889.
- (4) Zerweck, U.; Loppacher, C.; Otto, T.; Grafström, S.; Eng, L. M. *Phys. Rev. B* **2005**, *71*, 125424.
- (5) Charrier, D. S.; Kemerink, M.; Smalbrugge, B. E.; de Vries, T.; Janssen, R. A. *ACS Nano* **2008**, *2*, 622–626.
- (6) Melitz, W.; Shen, J.; Kummel, A. C.; Lee, S. *Surf. Sci. Rep.* **2011**, *66*, 1–27.
- (7) Sadeghi, A.; Baratoff, A.; Ghasemi, S. A.; Goedecker, S.; Glatzel, T.; Kawai, S.; Meyer, E. *Phys. Rev. B* **2012**, *86*, 075407.
- (8) Efron, B.; Tibshirani, R. J. *An introduction to the bootstrap*; CRC press, 1994.
- (9) Perdew, J. P.; Burke, K.; Ernzerhof, M. *Phys. Rev. Lett.* **1996**, *77*, 3865–3868.
- (10) Kresse, G.; Joubert, D. *Phys. Rev. B* **1999**, *59*, 1758–1775.
- (11) Kresse, G.; Hafner, J. *Phys. Rev. B* **1993**, *47*, 558–561.
- (12) Kresse, G.; Hafner, J. *Phys. Rev. B* **1994**, *49*, 14251–14269.
- (13) Kresse, G.; Furthmüller, J. *Comput. Mater. Sci.* **1996**, *6*, 15–50.
- (14) Kresse, G.; Furthmüller, J. *Phys. Rev. B* **1996**, *54*, 11169–11186.
- (15) Zhou, F.; Kang, K.; Maxisch, T.; Ceder, G.; Morgan, D. *Solid State Commun.* **2004**, *132*, 181 – 186.

- (16) Maxisch, T.; Zhou, F.; Ceder, G. *Phys. Rev. B* **2006**, *73*, 104301.
- (17) Henkelman, G.; Uberuaga, B. P.; Jónsson, H. *J. Chem. Phys* **2000**, *113*, 9901–5.
- (18) Dathar, G. K. P.; Sheppard, D.; Stevenson, K. J.; Henkelman, G. *Chem. Mater.* **2011**, *23*, 4032–4037.
- (19) Wang, L.; Zhou, F.; Meng, Y. S.; Ceder, G. *Phys. Rev. B* **2007**, *76*, 165435.
- (20) Paoletta, A.; Bertoni, G.; Hovington, P.; Feng, Z.; Flacau, R.; Prato, M.; Colombo, M.; Marras, S.; Manna, L.; Turner, S.; Van Tendeloo, G.; Guerfi, A.; P. Demopoulos, G.; Zaghbi, K. *Nano Energy* **2015**, *16*, 256–267.
- (21) Zaghbi, K.; Mauger, A.; Goodenough, J.; Gendron, F.; Julien, C. *Chem. Mater.* **2007**, *19*, 3740–3747.
- (22) Stevens, R.; Dodd, J.; Kresch, M.; Yazami, R.; Fultz, B.; Ellis, B.; Nazar, L. *J. Phys. Chem. B* **2006**, *110*, 22732–22735.